

Melt sonoquenching: an Affective Process to Obtain New Hybrid Material and Achieve Enhanced Electrochromic Performances Based on $V_2O_5/2,4,5$ -tris(1-methyl-4-pyridinium)-imidazolide Tetrafluoroborate Nanofibers

Renato S. de Oliveira, Juliana da S. Goulart, Fabio S. Miranda and Eduardo A. Ponzio*

Instituto de Química, Universidade Federal Fluminense, Outeiro de São João Batista S/No., 24020-141 Niterói-RJ, Brazil

Materiais electrocromicos híbridos são uma classe de compostos muito importantes para o desenvolvimento de novas tecnologias baseadas em propriedades ópticas e electroquímicas. Neste trabalho é relatada a síntese do novo híbrido $V_2O_5 \cdot 1,26H_2O([C_5N_2(C_6H_7N)_3])_{0,07}$ que utiliza a combinação de dois métodos tradicionais, o *melting quenching* e o sonoquímico. O material resultante foi caracterizado por diversos métodos a fim de verificar as características físicas e químicas e a sua possível utilização como electrodo electrocromico. O hóspede orgânico provoca uma diminuição do espaço entre as lamelas da matriz inorgânica e a interação electrostática entre os grupos oxo da matriz do V_2O_5 com os anéis piridínicos do hóspede orgânico demonstram uma forte interação. A nanoestrutura híbrida apresentou boa reversibilidade e ciclabilidade durante 50 ciclos, eficiência electrocromica de $22 \text{ cm}^2 \text{ C}^{-1}$ (410 nm) e 96% de retenção de coloração após os 50 ciclos de mudança de cor.

Hybrid electrochromic materials are a very important class of compounds, because they enable new and/or better optical and electrochemical properties to be unfolded. This paper reports the synthesis of the new $V_2O_5 \cdot 1,26H_2O([C_5N_2(C_6H_7N)_3])_{0,07}$ using the combination of two traditional methods, melting quenching and sonochemistry. The new material was characterized by several methods in order to verify the physical and chemical characteristics and its possible use as an electrochromic electrode. The organic guest provokes an interlayer spacing decrease of the inorganic matrix and the electrostatic interaction between the oxo groups of the V_2O_5 matrix and the pyridinium rings of the organic guest demonstrate a strong interaction. The new hybrid nanostructure presented good reversibility and cyclability during 50 cycles, electrochromic efficiency of $22 \text{ cm}^2 \text{ C}^{-1}$ (410 nm) and 96 % color retention after 50 cycles of color changing.

Keywords: electrochromic, hybrid materials, V_2O_5 , nanofibers, melt sonoquenching

Introduction

Hybrid organic-inorganic materials have been used to develop new technologies based on the combination of organic and inorganic building blocks to generate multifunctional materials. A common method of preparation of organic-inorganic hybrid materials is the intercalation of organic molecules into layered inorganic compounds as transition metals oxides.¹

The hybrid materials take advantage of the best properties of each component and have found applications in many fields such as optics, electronics, and others.²⁻⁵

Different transition metal oxides are used as hybrid matrixes, for example: TiO_2 ,⁶⁻¹¹ Fe_2O_3 ,^{12,13} MnO_2 ,¹⁴⁻¹⁶ WO_3 ,¹⁷⁻²¹ V_2O_5 ,^{2,22-24} and others.

Vanadium pentoxide (V_2O_5) xerogel has a versatile lamellar structure that can intercalate a wide variety of inorganic and organic guest species.^{25,26} Much effort has been made to produce new types of hybrid vanadium oxide/organic due to their potential applications in different fields such as: secondary batteries, catalysis, supercapacitor, thermochromism and electrochromism.^{27,28}

Electrochemical studies have shown that the performance of vanadium oxide films is directly related to its crystallinity, morphology, degree of disorder and other parameters related to the preparation methods. Significant

*e-mail: eaponzio@vm.uff.br

differences were reported on the potential and optical transmittance on thin films electrodes of amorphous and crystalline vanadium oxide.^{27,29}

V₂O₅ xerogels have lamellar (or 2D) structure suitable for intercalation reactions. For this reason, V₂O₅ xerogel has been regarded as a suitable host unit for organic-inorganic hybrid materials.

The strength of the intermolecular interactions between the organic guest and the inorganic matrix is responsible for the stability of the hybrid. Many studies have been performed to improve the properties of the polyaniline/V₂O₅ system.^{23,30-32} The polymeric component stabilizes the hybrid material probable due to a homogeneous distribution of the induced stress during cycling. Oliveira *et al.*³³ synthesized melanin/V₂O₅·nH₂O and polyaniline/V₂O₅·nH₂O hybrids. They demonstrated that the presence of either melanin or polyaniline between the vanadium oxide layers causes an increase in the interplanar distances. Additionally, they provided an increase of electronic and ionic conductivity, and improvements on the optical properties of the V₂O₅.

Several articles, dealing with the preparation of devices and multifunctional materials using V₂O₅ have been published.^{23,26,34-54} All the studies indicated that the performance of the hybrid is affected by the synthetic route.

The vanadium oxide hybrids can be prepared by various techniques, among them we can highlight the sol-gel method, hydrothermal synthesis, (or mixed method sol-gel/hydrothermal), sonochemistry, electrochemistry, chemical polymerization, melting quenching, among others.^{23,26,34-49}

The melting quenching presents some advantages as easy implementation and use of simpler and cheaper equipment, compared to sol-gel method or mixed method sol-gel/hydrothermal, electrochemistry, and others. Melting intercalation is commonly used for production of composites and nanocomposites, particularly with polymers⁵⁵⁻⁵⁷ but is little used for the synthesis of the inorganic matrix for inorganic/organic hybrids. The use of vanadium oxide in the production of electrochromic hybrids is of great importance due to the possibility of creating new optical and electrochemical properties, thus making of these hybrids an important source for the production of multicolored materials, with better response times, electrochromic and coulombic efficiencies, and greater transmittance variations when applying different electric potentials.

In this paper, we present a fast and easy route to produce a new nanostructured hybrid V₂O₅/2,4,5-tris(1-methyl-4-pyridinium)-imidazolidine nanofibers by a mixed method melt-quenching/sonochemistry (melt sonoquenching). The organic component is an unpublished molecule. This

novel hybrid has some special advantages: low-cost, good electrochromic response and the mixed method procedure is easily applicable for industrial purposes.

Experimental

Synthesis of 2,4,5-tris (1-methyl-4-pyridinium)-imidazolidetetrafluoroborate (TPI-Me(BF₄)₂)

All the reagents and solvents for synthesis and analysis were of analytical and/or spectroscopic grade and used without further purification. The 2,4,5-tris(4-pyridinyl)imidazole (Htpim) was prepared as described elsewhere.^{58,59}

A mixture of 200 mg (0.668 mmol) of Htpim and 0.5 mL (8.02 mmol) of methyl iodide in 9 mL of dimethylformamide (DMF) was heated at 100 °C with stirring for 15 h. After cooling to room temperature, ethyl acetate was added to the reaction mixture, the solid formed was filtered, washed with hexane resulting in an orange solid (293.8 mg, 78%). 200 mg (0.335 mmol) of 2,4,5-tris (1-methyl-4-pyridinium)-imidazolate iodide was dissolved in water and 130 mg (0.668 mmol) of AgBF₄ was added with stirring for 15 min. The AgI formed was filtered off and washed with distilled water. The filtrate was evaporated and the solid obtained was washed with ethyl ether resulting in a yellow solid (125.8 mg, 73%). ¹H NMR (DMSO-d₆, 500 MHz) δ: 9.00 (d, 2H, J₃ 6.7 Hz), 8.90 (d, 4H, J₃ 6.6 Hz), 8.58 (d, 2H, J₃ 6.9 Hz), 8.25 (d, 4H J₃ 6.9 Hz), 4.35 (s, 6H), 4.34 (s, 3H). ¹³C NMR (DMSO-d₆, 75 MHz): 146.0, 145.7, 143.3, 136.4, 125.3, 122.5, 54.6, 54.5, 47.5, 47.4.

Instrumentation

¹H and ¹³C NMR spectra were collected on a Varian AS400 spectrometer. Elemental analyses were carried out on a CHN Varian EA 1100.

Synthesis of the V₂O₅·nH₂O and hybrid material

Vanadium pentoxide xerogel (V₂O₅·nH₂O) and hybrid material were synthesized through melt quenching assisted with ultrasound (melt sonoquenching) using ammonium metavanadate (NH₄VO₃) as precursor. In a porcelain crucible 2.0 g de NH₄VO₃ was added, and heated at 800 °C during 1 h. After this step, the liquid formed was immediately spilled into 20.0 mL in a saturated aqueous TPI-Me(BF₄)₂ at room temperature under the influence of an ultrasound probe (Sonics Vibra-cell 130 W and 20 kHz-Probe No.630-0435) during 1 h. The procedure of spilled of V₂O₅ liquid into a becker with the TPI-Me(BF₄)₂

is with the aid of a claw 50 cm and using all necessary personal protective equipment. The hybrid material was left ageing for 7 days without stir and, at the end of this time, the gel produced was centrifuged and washed several times with ethanol and then dried at 110 °C for 24 h.

The material was deposited in indium tin oxide (ITO) substrate using spin-coating technique. The spin-coater used is homemade equipment; all parameter (rpm, time, concentration of suspension and volume apply) was the same for all materials studies for maintain the same geometric area, uniformity surface and film thickness. For all the depositions, it was used 1000 rpm, 1 min and 10 drops of a suspension of the materials (50 mg mL⁻¹ in acetonitrile). The exposed area was 0.84 cm². The resulting electrodes were allowed to 110 °C for 24 h.

Materials and methods

The crystalline structure of the powders was analyzed by X-ray powder diffraction (XRD). The diffractometer used was a Bruker AXS D8 Advance (Cu K_α radiation, 40 kV and 40 mA) with LynxEye detector. The diffraction patterns were collected in a flat geometry with steps of 0.02° and accumulation time of 0.5 s per step.

Fourier transform infrared spectroscopy (FT-IR) measurements were taken in a Varian 660-FTIR spectrometer.

Thermal analyses were performed in a Shimadzu TGA-60, using a heating rate of 5 °C min⁻¹ from room temperature to 600 °C in N₂ with a flow rate of 50 mL min⁻¹.

Surface morphology was investigated using a Jeol JSM-6701F scanning electron microscope (SEM). The accelerating voltage was preset at 5 kV. Imaging was obtained by a backscattering electron detector with the preset charge-up reduction mode. Jeol software was used to control the instrument.

Atomic force microscopy (AFM) were taken in a Nanosurf Flex AFM. The hybrid material was deposited on a Si substrate and images were acquired in tapping mode under ambient conditions, using the Nanosurf easyScan 2 Flex AFM scanner and cantilever type PPP-NCLR (Nanosensors).

A potentiostat/galvanostat Microautolab Type III and a spectrophotometer Ocean Optics USB650UV were used for the spectroelectrochemical measurements. The electrochemical cell was composed of a quartz cuvette with 1 cm optical path containing three electrodes. The working electrode was glass covered with ITO with the composite deposited on a conducting surface using the technique of spin-coating, the counter electrode was a Pt wire and the quasi-reference electrode was a silver wire coated with AgCl. A solution of 0.5 mol L⁻¹ LiClO₄ in acetonitrile was used as electrolyte. The optical and electrochemical measurements were carried out at room temperature.

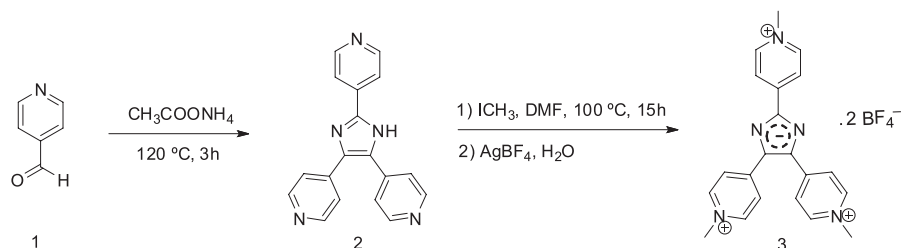
Results and Discussion

Synthesis and characterization of TPI-Me(BF₄)₂

The synthesis of TPI-Me(BF₄)₂ is straight forward, the Scheme 1 shows the synthetic route. Htpim was prepared as described by Proskurnina *et al.*^{58,59} followed by the alkylation⁶⁰ of the pyridines resulting in the TPI-Me diiodide with yield of 78% (see Scheme 1). The exchange of the anion by salt metathesis reaction can be verified by the infrared spectrum, which has the characteristic BF₄⁻ band at 1050 cm⁻¹. The deprotonating of the imidazole is due to the weakness of the N–H bond caused by the strong electron-withdrawing effect of the three cationic pyridyl groups connected to each carbon of the imidazole ring. In this case, the water molecules from the metathesis solution keep the media alkaline enough to remove the imidazole proton. The synthesized compounds were analyzed by ¹H NMR spectroscopy and ¹³C (Supporting Information).

Hybrid material

The melt sonoquenching synthesis used in the production of vanadium oxide is based on heating the vanadium oxide at temperatures above its melting point with subsequent abrupt cooling to room temperature. The heating at 800 °C of the NH₄VO₃ for 1 h was enough for the precursor total decomposition, forming the vanadium pentoxide, according to reaction 1. The melting point of the



Scheme 1. Synthetic route for the synthesis of TPI-Me(BF₄)₂.

vanadium oxide occurs at a temperature of 670 °C, forming vanadium oxide in liquid state, according to reaction 2. When turning the liquid vanadium oxide into saturated solution of TPI-Me(BF₄)₂ under ultrasonic processors at room temperature, a gel is immediately formed with a green-orange color, according to reaction 3. The green-orange color is because the incorporation of TPI-Me²⁺ that induces the reduction of part of V⁺⁵ to V⁺⁴.



The influence of ultrasonic irradiation on heterogeneous media is complex since it may involve several physical and chemical processes, such as the production of microstreaming, microstreamers, microjets, shock waves reactive free radicals, mass transfer, enormous local temperatures and pressures, mixing, solid erosion, all associated with the process of cavitation.⁶¹⁻⁶⁶

Currently, the influence of TPI-Me²⁺ and the mechanism of formation of the hybrid nanofibers are still under investigation. Apparently, the use of the ultrasonic bath in the cooling process impairs crystal growth, since the uniform and fast cooling creates a kinetic condition unfavorable to the occurrence of recrystallizations during cooling. The reactions induced by low frequency ultrasound, more violent cavitation, resulting in higher localized temperatures and pressure improve the intercalation of the organic compound.

XRD measurements of the matrix intercalation (V₂O₅·nH₂O xerogel) and the hybrid material were performed, and are shown in Figure 1. The XRD pattern of the matrix indicates the presence of the peak at 2θ = 6.2° for the (001) diffraction plane, as expected for a layered material with the layers parallel to the reflection plane, corresponding to the interlayer distance of 14.2 Å, which is consistent with data found in the literature.⁶⁷⁻⁶⁹ It is possible to observe a second peak at 2θ = 26° for the (003) diffraction plane, according to the literature.^{26,33,70,71}

It is important to note also that the X-ray diffraction pattern is characteristic of an amorphous material. Diffraction pattern of the hybrid material, Figure 1b, shows the same peak of matrix at 2θ = 26°, but it shows a diffraction peak at 2θ = 7.2° for the (001) diffraction plane, corresponding to the interlayer distance of 12.2 Å.

The interlayer spacing decreases from 14.2 Å to 12.2 Å. This might correspond to water expulsion and to the thickness of TPI-Me²⁺ molecules lying flat between V₂O₅

ribbons. As shown in Figure 1a and b, the relative intensities of the (001) diffraction plane of V₂O₅ (I₀₀₁/I₁₁₀ = 3.0) and hybrid (I₀₀₁/I₁₁₀ = 2.9) are similar. The hybrid presents strong (001) reflexions as one would expect for a well-organized intercalation compound. The increase of the crystallinity of hybrid materials has also been observed elsewhere.^{33,70} This is a clear indication that the 1D order along the c* axis of the material is not lost. Nevertheless, our XRD data will obviously need confirmation by other techniques.

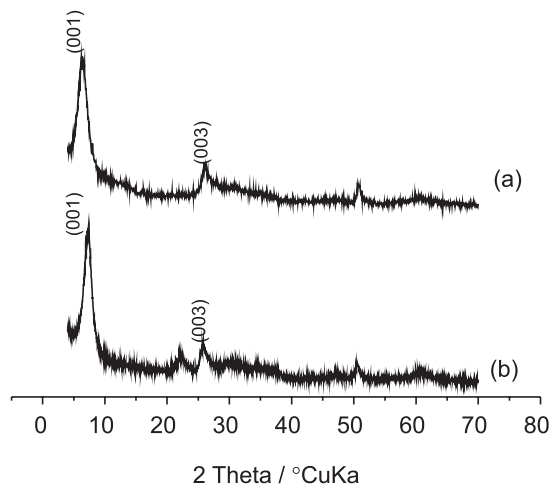


Figure 1. XDR for V₂O₅·nH₂O xerogel in (a) and hybrid material in (b).

It is noteworthy that these interlamellar distances are relative, because they are directly dependent on the new composition of hybrid materials produced. So, in order to verify the composition and thermal stability, the hybrid material synthesized was characterized through thermogravimetric measures, according to Figure 2.

Figure 2a presents the thermogram of V₂O₅·nH₂O xerogel where two regions of weight loss can be observed. The first weight loss extends to 130 °C and is related to the loss of absorbed water interlayer of vanadium oxide. The second weight loss, of less intensity, occurs from 320 to 360 °C and is attributed to the release of water molecules coordinated to the vanadyl group and molecules present in the plane of the lamella.⁷¹ The probable composition of the intercalation matrix is V₂O₅·2.8H₂O.

Figure 2b shows the thermogram of the intercalating TPI-Me(BF₄)₂. It is possible to check a very intense weight loss in three consecutive steps, starting at 180 °C and extending up to 600 °C, related to the decomposition of the TPI-Me(BF₄)₂. In the thermogram of the hybrid, Figure 2c, there is an initial weight loss extending up to 130 °C related to water loss and a second weight loss that occurs from 290 to 430 °C is due to the decomposition of the TPI-Me(BF₄)₂ interlayer.

The composition was determined to be $V_2O_5 \cdot 1.26H_2O \cdot ([C_3N_2(C_6H_7N)_3])_{0.07}$ based on the consecutive weight loss of water and polymer, i.e., $V_2O_5 \cdot yH_2O \cdot (TPI-Me)_x \rightarrow V_2O_5 \cdot (TPI-Me)_x \rightarrow V_2O_5$.

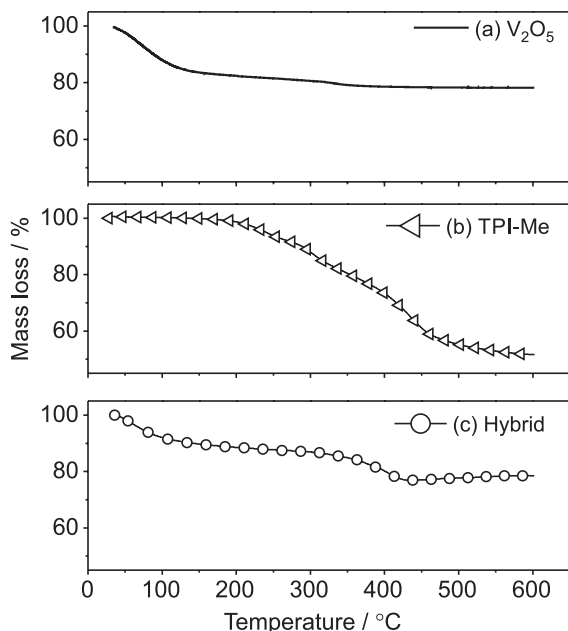


Figure 2. Thermal analyses measurements for $V_2O_5 \cdot nH_2O$ in (a), TPI-Me(BF_4)₂ in (b) and hybrid in (c).

The FT-IR spectra of V_2O_5 xerogel, TPI-Me(BF_4)₂ and TPI-Me/ V_2O_5 hybrid are shown in Figure 3. The characteristic bands of V_2O_5 xerogel are clearly observed in Figure 3a specifically, the three absorption bands centered at 535, 798 and 995 cm^{-1} assigned to symmetric and asymmetric stretching modes of V–O–V (ν_{sy} and ν_{asy}) and symmetric stretching mode of the V=O (ν_s), respectively.⁷²

The infrared spectrum of TPI-Me(BF_4)₂ (Figure 3b), shows a band at 854 cm^{-1} assigned to the C–H out-of-plane bending vibration of pyridinium rings. The doublet at ca. 1039–1059 cm^{-1} confirms the π ion in the structure.⁷³ The bands at 1365 and 1435 cm^{-1} are attributed to $\nu(C=N)$, 1635 and 1737 cm^{-1} to $\nu(C-C_{aromatic})$, 2970 cm^{-1} $\nu(C-H_{aliphatic})$ and 3025 cm^{-1} $\nu(C-H_{aromatic})$.

For the TPI-Me/ V_2O_5 hybrid (Figure 3c), the intercalation of TPI-Me²⁺ is evidenced by the presence of the TPI-Me²⁺ peaks between 1000–3200 cm^{-1} . The V–O–V vibration at 798 cm^{-1} (V_2O_5) shifted to 748 cm^{-1} (TPI-Me/ V_2O_5), indicating a strong electrostatic interaction between V_2O_5 and TPI-Me²⁺. The vanadyl V=O vibration band at 995 cm^{-1} in the V_2O_5 xerogel shifted to 985 cm^{-1} upon intercalation of TPI-Me²⁺ into V_2O_5 . This shift suggests a strong interaction between vanadyl group and the incorporated TPI-Me²⁺. The characteristic absorption band of the π ion disappeared in the hybrid suggesting that the intercalated TPI-Me²⁺ in the

oxide matrix is stabilized by the anionic nature of the V_2O_5 . This is confirmed by the shift of the $\nu(C=N)$ bands to lower wavenumbers in the TPI-Me/ V_2O_5 hybrid, that confirm the electrostatic interaction between the oxo groups from the V_2O_5 matrix and the pyridinium rings of the organic guest. All these interactions between V_2O_5 and TPI-Me confirm the interlayer spacing decrease as shown in the XRD results.

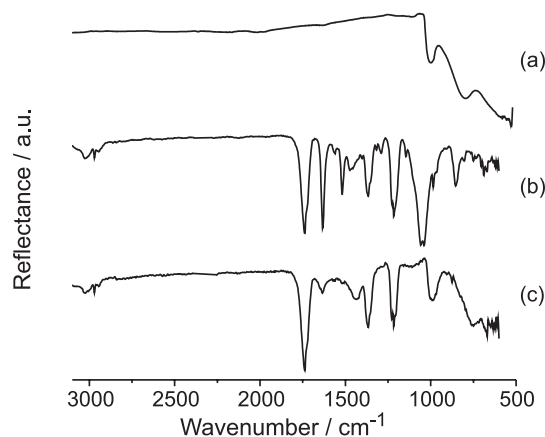


Figure 3. FT-IR spectra for intercalation matrix in (a), for intercalated in (b) and for hybrid in (c).

The hybrid was characterized by SEM and AFM, as shown in Figure 4a and b respectively. There is an aggregate fibrous morphology. In Figure 4b, a fiber medium length of 300 nm and medium width of 30 nm. The film thickness is determined by AFM ca. 112 nm. It is also found that these submicrosized particles are aggregates made of much smaller nanofibers.

In order to understand the effect of the incorporation into V_2O_5 in the electrochemical performance electrochemical experiments as cyclic voltammetry (CV) and chronoamperometry method with UV-Vis *in situ* were carried out.

The CV experiment (Figure 5), under conditions of continuous potentiodynamic cycling at a scan rate of 10 $mV s^{-1}$, started from open circuit potential (0.38 V vs. Ag), scanning in the positive direction until 1.2 V and then, scanning in the negative direction until –0.6 V. The CV is very similar to that of V_2O_5 xerogel, with two well-defined anodic peaks at 0.14 V and at 0.56 V (vs. Ag), these waves are ascribed to the V^{4+} to V^{5+} , presumably due to the Li^+ deinsertion in two non-equivalent sites in the vanadium oxide matrix. This first cycle confirms that the green-orange color is caused by the incorporation of TPI-Me²⁺ which induces the reduction V^{5+}/V^{4+} . In the reduction process, broad peaks localized at 0.27 V and at –0.49 V are observed and correspond to the intercalation of Li^+ . After 10 cycles, a little decrease of anodic and cathodic current is observed, which corresponds to the organization

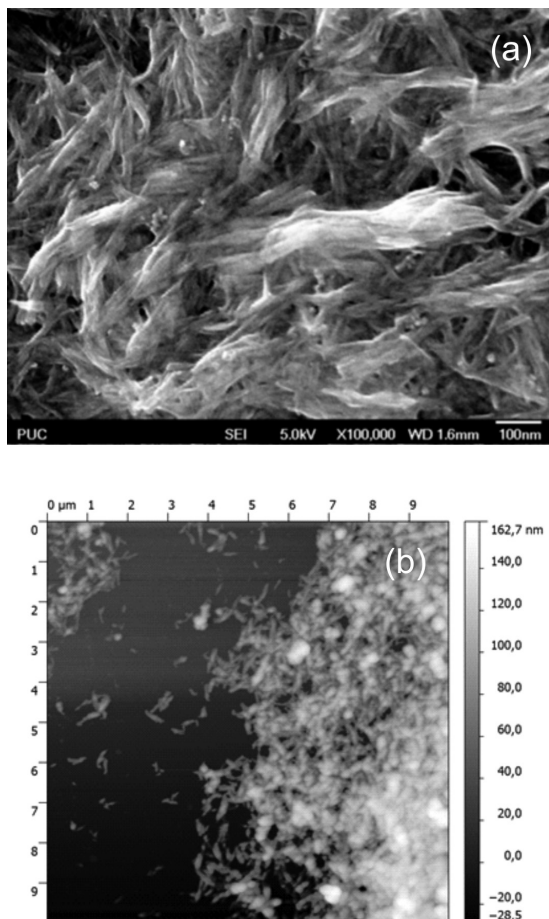


Figure 4. SEM image in (a) and AFM image in (b).

of layers of V_2O_5 when Li^+ is intercalated. The TPI-Me $^{2+}$ is electrochemically active (support information), but in the hybrid, the organic part apparently does not contribute to the overall redox process in the potential range used.

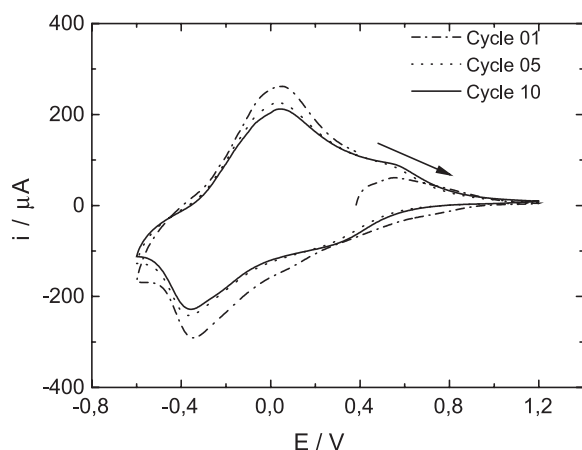


Figure 5. Cyclic voltammograms of hybrid material.

It must be noticed that, as a consequence of the synergistic effect between the two components, the

hybrid with fiber shape is electroactive in this range of potential.

The color transitions have been further investigated by recording the film absorption spectra at controlled potential. The vanadium oxide xerogel in a yellow-colored state may be converted to a green and/or blue-colored state upon inserting and extracting ions and electrons. It is observed an absorption band at 410 nm that is related to the transfer process the ligand-to-metal charge transfer (LMCT) transition of O^{2-} to V^{5+} and d-d transition of V^{4+} in the range of 530-850 nm, which is consistent with data from Gao *et al.*⁷⁴ and Liu *et al.*⁷⁵

Figure 6 shows the inspected UV-Vis spectra when applying a series of potential differences using chronoamperometry considering every spectrum was inspected when the current found its stability. UV-Vis spectroscopy was used to investigate the oxidation state changes of the hybrid. At -0.6 V (coloration state) it presents two absorption peaks, one with large absorption at 338 nm and another large peak at ca. 700 nm. The region 400-1000 nm corresponds to the d-d transition that occurs for V (+4) in the V_2O_5 matrix and the strong peak at 340 nm is assigned to the π - π^* transition of the piridinium ring.

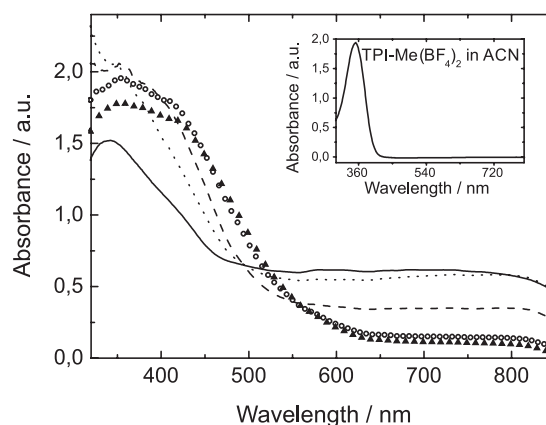


Figure 6. UV-Vis spectra when applying a series of potential differences: — -0.6 V; --- -0.2 V; ··· 0.2 V; -·-·- 1.0 V and \blacktriangle 1.2 V. Figure inside shows the absorption peak at 348 nm for the bulk TPI-Me(BF_4) $_2$ (in ACN).

When more positive potential is applied the peak of the π - π^* transition of the piridinium ring is shifted by 18 nm to a longer wavelength (358 nm). When applied potential, imposing 1.2 V (bleaching state), two bands are observed, at 348 nm (π - π^* transition of the piridinium ring) and at 410 nm assigned to transference for the V (+5) in the inorganic matrix; according to Ryczkowsky⁷⁶ the load transference of the binder to the metal (LMTC).

Figure 7 shows the variation of potential, absorbance and intensity in a 3D graph. Over the region from 540 to 850 nm, the absorption of the d-d transition of V_2O_5

decreases from 0.60 to around zero with potential increase; the absorption intensity increases from 1.00 to 1.70 for the LMCT transition and the π - π^* transition of the organic compound shows an increase, from 1.00 (-0.6V) to 2.00 (0.2 V) and a decrease from 2.00 (0.2 V) to 1.78 (1.2 V) followed by a wavelength shift from 340 (-0.6 V) to 358 (1.2 V) nm.

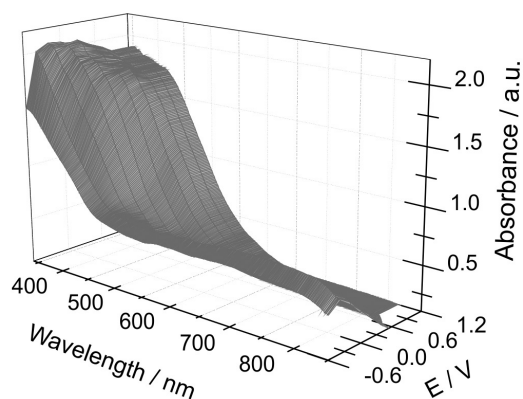


Figure 7. Variation of potential, absorbance and wavelength in a 3D graph.

Vanadium oxide undergoes structural modification during the Li^+ insertion process induced by mechanical stress leading.²³ These structural modifications arise from a variety of sources such as solvent transport into or out of the material during redox cycling, volumetric changes due to the electrochemical intercalation/deintercalation of Li^+ and changes in the coordination geometry at the metal center that result from the redox transition. When lithium is deintercalated (1.2 V) results in increased interlamellar separation and leads to a decrease in steric and electrostatic effects promoted by the higher interlamellar distance; in this situation the organic compound improves the effective degree of π -electron delocalization of the piridinium rings and increases the intensity of the π - π^* transition. On the other hand, when Li^+ is intercalated (-0.6 V) results in decreased interlamellar separation and leads to a reduction of the partial charge of the N in the piridinium ring, therefore reducing the intensity of the π - π^* transition.

Other electrochromic parameters were studied, such as response time, efficiency and reversibility. Chronoamperometric analysis (Figure 8) was also carried out, with follow-up of optical density variations *in situ*, using a 450 and 700 nm wavelength, in which there was a successive application of -0.6 V for 60 s and 1.2 V for 60 s, and the evolution of color variation on the material could be observed as a result of the cycles. It was also noted that the optical density (OD) variation *in situ* was 0.73 (450 nm) in the first cycle and increased to 1.09 in the last cycle.

According to the analysis, after 50 cycles ΔOD increased 43.6%. At 700 nm the ΔOD showed a little reduction of 4%.

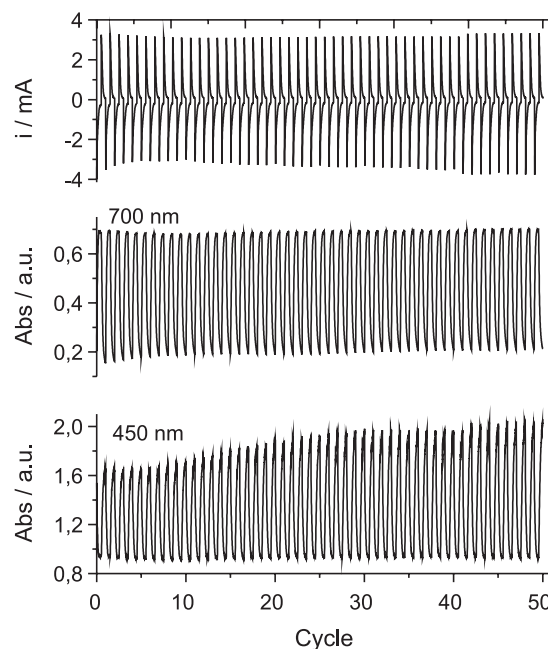


Figure 8. Chronoamperometric analysis and *in situ* optical density variation at 450 and 700 nm wavelength.

The electrochromic response time (t) is the time necessary for the material to change color, although there is no specific criterion to determine this response time, it can be obtained by the total transmittance variation (or absorbance) or by a fraction of this.⁷⁷ In this study, the response time calculation was defined as the necessary time from the beginning of the pulse until it reaches 50% of the total transmittance or absorbance variation of each pulse. In analyzing the response times necessary for the oxidation and reduction of the material a significant difference between them can be noticed. The response time of the reduction (around 12 s) was always higher than the response time for the oxidation (less than 5 s) throughout the 100 cycles, indicating that the V_2O_5 film takes approximately 2.4 times longer to reach the reduced state than to reach the oxidized state,⁷⁸ reported the color-switching time of vanadium oxide nanofibers to be 5 s and 6 s from the bleached state to the colored state and from the colored state to the bleached state. Cao *et al.*⁷⁹ reported that a 30% transmittance change at 700 nm took 50 s for a V_2O_5 nanorod, and 300 s was required for a sol-gel V_2O_5 . For electrochromic applications, immediate color-switching is very important. The rates of coloring and bleaching depend on the lithium ion diffusion and are related to the distance in the interlayer space of the nanofibers. In our case, the hybrid nanofibers are 30 nm wide, which provides a short diffusion distance, but the TPI-Me^{2+} charge difficults the

diffusion of Li^+ in the inorganic matrix, therefore the hybrid presents a long response time.

The electrochromic and coulombic efficiencies were calculated. The electrochromic efficiency was $22 \text{ cm}^2 \text{ C}^{-1}$ (700 nm) and the coulombic efficiency for the first and fiftyth cycles were 0.94 and 0.97, respectively. At 450 nm the electrochromic efficiency was $14 \text{ cm}^2 \text{ C}^{-1}$ and the coulombic efficiency the same as at 700 nm.

An essential characteristic that must be searched in these types of materials is their electrochromic stability, because they are subjected to multiple intercalation/deintercalation of Li^+ . The hybrid nanofibers shown in this work exhibited good long-term cycle stability; at 450 nm the ΔOD increased from 0.72 to 1.12 and at 700 nm there was less than 4% drop in coloration contrast after 50 switching cycles. These results demonstrate a substantial improvement in cycling efficiency of the hybrid, and that the insertion of the TPI- Me^{2+} into the inorganic matrix resulted in an assembled hybrid structure which led to the stabilization of the electrochromic response.

Conclusion

This contribution demonstrates that it is possible to obtain an inedited hybrid nanomaterial using the mixed technique, melting quenching and ultrasound. This hybrid, with defined morphology, can be used as electroactive material in electrochromic electrodes. In the proposed method of synthesis, it is possible to obtain a hybrid with 0.07 mol of TPI- Me^{2+} per mol of V_2O_5 . The experimental tools used allowed the characterization of the morphology and local structure showing that the TPI- Me^{2+} causes an interlayer spacing decrease of the inorganic matrix and the electrostatic interaction between the oxo groups from the V_2O_5 matrix and the pyridinium rings of organic guest demonstrates a strong interaction. These new hybrid nanostructures improve the electrochromic performance, as it was shown by using spectroelectrochemical analysis. After 50 cycles the ΔOD increased 43.6%. At 700 nm the ΔOD showed a little reduction of 4%. The hybrid exhibited good long-term cycle stability, at 450 nm the ΔOD increased 43.6% and at 700 nm with less than 4% drop in coloration contrast after 50 switching cycles, the electrochromic efficiencies were $22 \text{ cm}^2 \text{ C}^{-1}$ (700 nm) and $14 \text{ cm}^2 \text{ C}^{-1}$ (450 nm), and the coulombic efficiency was 97%, indicating that this hybrid possesses great potential to be used in electrochromic electrodes.

Supplementary Information

Supplementary data are available free of charge at <http://jbcbs.sbq.org.br> as PDF file.

Acknowledgments

The authors are grateful to the Coordenação de Aperfeiçoamento de Pessoal de Nível Superior (CAPES), Fundação Carlos Chagas de Amparo a Pesquisa do Estado do Rio de Janeiro (FAPERJ, E-26/102.971/2012 and E-26/111.407/2013), and Pró-reitoria de Pesquisa, Pós-graduação e Inovação (Proppi-UFF) for constant financial support and to Professor Jackson Antonio Lamounier Camargos Resende and LDRX-UFF for the XRD measurements.

References

1. Kang, S.-G.; Kim, K. M.; Park, N.-G.; Ryu, K. S.; Chang, S.-H.; *J. Power Sources* **2004**, *133*, 263.
2. Gomez-Romero, P.; *Adv. Mater.* **2001**, *13*, 163.
3. Ferreira, M.; Zucolotto, V.; Constantino, C. J. L.; Temperini, M. L. A.; Torresi, R. M.; Oliveira Jr, O. N.; *Synth. Met.* **2003**, *137*, 969.
4. Loy, D. A.; Shea, K. J.; *Chem. Rev.* **1995**, *95*, 1431.
5. Sanchez, C.; Julian, B.; Belleville, P.; Popall, M.; *J. Mater. Chem.* **2005**, *15*, 3559.
6. Schnitzler, D. C.; Zarbin, A. J. G.; *J. Braz. Chem. Soc.* **2004**, *15*, 378.
7. Nogueira, A. F.; Micaroni, L.; Gazotti, W. A.; De Paoli, M.-A.; *Electrochem. Commun.* **1999**, *1*, 262.
8. Murakoshi, K.; Kogure, R.; Wada, Y.; Yanagida, S.; *Chem. Lett.* **1997**, *26*, 471.
9. Murakoshi, K.; Kogure, R.; Wada, Y.; Yanagida, S.; *Sol. Energy Mater. Sol. Cells* **1998**, *55*, 113.
10. Wang, G.; Chen, H.; Zhang, H.; Yuan, C.; Lu, Z.; Wang, G.; Yang, W.; *Appl. Surf. Sci.* **1998**, *135*, 97.
11. Kobayashi, N.; Teshima, K.; Hirohashi, R.; *J. Mater. Chem.* **1998**, *8*, 497.
12. Bidan, G.; Jarjays, O.; Fruchart, J. M.; Hannecart, E.; *Adv. Mater.* **1994**, *6*, 152.
13. Wan, M.; Zhou, W.; Li, J.; *Synth. Met.* **1996**, *78*, 27.
14. Kuwabata, S.; Kisimoto, A.; Tanaka, T.; Yoneyama, H.; *J. Electrochem. Soc.* **1994**, *141*, 10.
15. Yoneyama, H.; Kishimoto, A.; Kuwabata, S.; *J. Chem. Soc., Chem. Commun.* **1991**, 986.
16. Gemeay, A. H.; Nishiyama, H.; Kuwabata, S.; Yoneyama, H.; *J. Electrochem. Soc.* **1995**, *142*, 4190.
17. Yoneyama, H.; Shoji, Y.; *J. Electrochem. Soc.* **1990**, *137*, 3826.
18. Yoneyama, H.; Hirao, S.; Kuwabata, S.; *J. Electrochem. Soc.* **1992**, *139*, 3141.
19. Shen, P. K.; Huang, H. T.; Tseung, A. C. C.; *J. Electrochem. Soc.* **1992**, *139*, 1840.
20. Jelle, B. P.; Hagen, G.; Noedland, S.; *Electrochim. Acta* **1993**, *38*, 1497.

21. Avvaru, N. R.; Rajeshwar, K.; *Analyst* **1998**, *123*, 113.
22. Shi, Z.; Zhang, L.; Zhu, G.; Yang, G.; Hua, J.; Ding, H.; Feng, S.; *Chem. Mater.* **1999**, *11*, 3565.
23. Ponzio, E. A.; Benedetti, T. M.; Torresi, R. M.; *Electrochim. Acta* **2007**, *52*, 4419.
24. Hagrman, P. J.; Zubieta, J.; *Inorg. Chem.* **2001**, *40*, 2800.
25. Wang, Y.; Cao, G.; *Chem. Mater.* **2006**, *18*, 2787.
26. Zampronio, E. C.; Greggio, D. N.; Oliveira, H. P.; *J. Non-Cryst. Solids* **2003**, *332*, 249.
27. Oliveira, M. R. S.; Mello, D. A. A.; Oliveira, R. S.; Ponzio, E. A.; Oliveira, S. C. In *Advances in Nanotechnology*; Bartul, Z.; Trenor, J., eds.; Nova Publishers: New York, 2011, Vol. 8, p. 1.
28. Bazito, F. F. C.; Fiorito, P. A.; Ponzio, E. A.; Vidotti, M.; Torresi, S. I. C.; Torresi, R. M. In *Handbook of Organic Electronics and Photonics*; Nalwa, H. S., ed.; American Scientific Publishers: California, 2008; Vol. 3, p. 51.
29. Scarminio, J.; Talledo, A.; Andersson, A. A.; Passerini, S.; Decker, F.; *Electrochim. Acta* **1993**, *38*, 1637.
30. Leroux, F.; Koene, B. E.; Nazar, L. F.; *J. Electrochem. Soc.* **1996**, *143*, L181.
31. Kuwabata, S.; Idzu, T.; Martin, C. R.; Yoneyama, H.; *J. Electrochem. Soc.* **1998**, *145*, 2707.
32. Lira-Cantu, M.; Gomez-Romero, P.; *J. Electrochem. Soc.* **1999**, *146*, 2029.
33. Oliveira, H. P.; Graeff, C. F. O.; Brunello, C. A.; Guerra, E. M.; *J. Non-Cryst. Solids* **2000**, *273*, 193.
34. Boyano, I.; Bengoechea, M.; de Meatza, I.; Miguel, O.; Cantero, I.; Ochoteco, E.; Rodriguez, J.; Lira-Cantu, M.; Gomez-Romero, P.; *J. Power Sources* **2007**, *166*, 471.
35. Malta, M.; Louarn, G.; Errien, N.; Torresi, R. M.; *J. Power Sources* **2006**, *156*, 533.
36. Anaissi, F. J.; Engelmann, F. M.; Araki, K.; Toma, H. E.; *Solid State Sci.* **2003**, *5*, 621.
37. Wang, G.; Zhao, J.; Li, X.; Li, C.; Yuan, W.; *Synth. Met.* **2009**, *159*, 366.
38. Boyano, I.; Bengoechea, M.; de Meatza, I.; Miguel, O.; Cantero, I.; Ochoteco, E.; Grande, H.; Lira-Cantu, M.; Gomez-Romero, P.; *J. Power Sources* **2007**, *174*, 1206.
39. Guerra, E. M.; Ciuffi, K. J.; Oliveira, H. P.; *J. Solid State Chem.* **2006**, *179*, 3814.
40. Kwon, C.-W.; Vadivel, M. A.; Campet, G.; Portier, J.; Kale, B. B.; Vijaymohan, K.; Choy, J.-H.; *Electrochem. Commun.* **2002**, *4*, 384.
41. Wu, C.-G.; Chung, M.-H.; *J. Solid State Chem.* **2004**, *177*, 2285.
42. Huguenin, F.; Ticianelli, E. A.; Torresi, R. M.; *Electrochim. Acta* **2002**, *47*, 3179.
43. Ren, X.; Shi, C.; Zhang, P.; Jiang, Y.; Liu, J.; Zhang, Q.; *Mater. Sci. Eng., B* **2012**, *177*, 929.
44. Huguenin, F.; Torresi, R. M.; *J. Phys. Chem. C* **2008**, *112*, 2202.
45. Malta, M.; Torresi, R. M.; *Electrochim. Acta* **2005**, *50*, 5009.
46. Huguenin, F.; Torresi, R. M.; *Quim. Nova* **2004**, *27*, 393.
47. Soltane, L.; Sediri, F.; *Ceram. Int.* **2013**, *40*, 1531.
48. Soltane, L.; Sediri, F.; *Mater. Sci. Eng., B* **2013**, *178*, 502.
49. Oliveira, R. S.; Alves, W. A.; Ponzio, E. A.; *ECS Trans.* **2012**, *43*, 363.
50. Cao, Z.; Wei, B.; *Nano Energy* **2013**, *2*, 481.
51. Mohd Yusoff, A. R. B.; Kim, H. P.; Jang, J.; *Org. Electron.* **2013**, *14*, 858.
52. Wang, S.; Kang, Y.; Wang, L.; Zhang, H.; Wang, Y.; Wang, Y.; *Sens. Actuators, B* **2013**, *182*, 467.
53. Guo, H.; Liu, L.; Wei, Q.; Shu, H.; Yang, X.; Yang, Z.; Zhou, M.; Tan, J.; Yan, Z.; Wang, X.; *Electrochim. Acta* **2013**, *94*, 113.
54. Wung, C. J.; Wijekoon, W. M. K. P.; Prasad, P. N.; *Polymer* **1993**, *34*, 1174.
55. Liu, X.; Wu, Q.; *Polymer* **2001**, *42*, 10013.
56. Wang, S.; Long, C.; Wang, X.; Li, Q.; Qi, Z.; *J. Appl. Polym. Sci.* **1998**, *69*, 1557.
57. Kumar, S.; Jog, J. P.; Natarajan, U.; *J. Appl. Polym. Sci.* **2003**, *89*, 1186.
58. Lozinskaya, N. A.; Tsybezova, V. V.; Proskurnina, M. V.; Zefirov, N. S.; *Russ. Chem. Bull.* **2003**, *52*, 674.
59. Proskurnina, M. V.; Lozinskaya, N. A.; Tkachenko, S. E.; Zefirov, N. S.; *Russ. J. Org. Chem.* **2002**, *38*, 1149.
60. Alcalde, E.; Dinares, I.; Frigola, J.; Jaime, C.; Fayet, J. P.; Vertut, M. C.; Miravittles, C.; Rius, J.; *J. Org. Chem.* **1991**, *56*, 4223.
61. Chen, D. In *Handbook on Applications of Ultrasound: Sonochemistry for Sustainability*; Chen, D.; Sharma, S. K.; Mudhoo, A., eds.; CRC Press: 2011, p 739.
62. Thompson, L. H.; Doraiswamy, L. K.; *Ind. Eng. Chem. Res.* **1999**, *38*, 1215.
63. Adewuyi, Y. G.; *Ind. Eng. Chem. Res.* **2001**, *40*, 4681.
64. Gedanken, A.; *Ultrason. Sonochem.* **2004**, *11*, 47.
65. Kuppa, R.; Moholkar, V. S.; *Ultrason. Sonochem.* **2010**, *17*, 123.
66. Wu, T. Y.; Guo, N.; Teh, C. Y.; Hay, J. X. W.; *Advances in Ultrasound Technology for Environmental Remediation*, 1st ed; Springer: Cham, CH, 2013.
67. Pyun, S.-I.; Bae, J.-S.; *J. Power Sources* **1997**, *68*, 669.
68. Arashiro, E.; Zampronio, E. C.; Brunello, C. A.; Lassali, T. A. F.; Oliveira, H. P.; Graeff, C. F. O.; *Int. J. Inorg. Mater.* **2001**, *3*, 727.
69. Park, N.-G.; Ryu, K. S.; Park, Y. J.; Kang, M. G.; Kim, D.-K.; Kang, S.-G.; Kim, K. M.; Chang, S.-H.; *J. Power Sources* **2002**, *103*, 273.
70. Oliveira, H. P.; Graeff, C. F. O.; Zanta, C. L. P. S.; Galina, A. C.; Goncalves, P. J.; *J. Mater. Chem.* **2000**, *10*, 371.
71. Oliveira, H. P.; Graeff, C. F. O.; Rosolen, J. M.; *Mater. Res. Bul.* **1999**, *34*, 1891.
72. Leroux, F.; Goward, G.; Power, W. P.; Nazar, L. F.; *J. Electrochem. Soc.* **1997**, *144*, 3886.
73. Bonadeo, H.; Silberman, E.; *J. Mol. Spectrosc.* **1969**, *32*, 214.

74. Gao, X.; Banares, M. A.; Wachs, I. E.; *J. Catal.* **1999**, *188*, 325.
75. Liu, J.; Zhao, Z.; Xu, C.; Duan, A.; Zhu, L.; Wang, X.; *Catal. Today* **2006**, *118*, 315.
76. Ryczkowski, J.; *Catal. Today* **2001**, *68*, 263.
77. Chary, K. V. R.; Kumar, C. P.; Naresh, D.; Bhaskar, T.; Sakata, Y.; *J. Mol. Catal. A: Chem.* **2006**, *243*, 149.
78. Cheng, K.-C.; Chen, F.-R.; Kai, J.-J.; *Sol. Energy Mater. Sol. Cells* **2006**, *90*, 1156.
79. Takahashi, K.; Wang, Y.; Cao, G.; *Appl. Phys. Lett.* **2005**, *86*, 53102.

Submitted on: September 5, 2013
Published online: February 7, 2014